E 2 Modeling blood flow and primary hemostasis in microcirculation

D. A. Fedosov

Theoretical Soft Matter and Biophysics

Institute of Complex Systems

Forschungszentrum Jülich GmbH

Contents

Lecture Notes of the 49^{th} IFF Spring School "Physics of Life" (Forschungszentrum Jülich, 2018).

1 Introduction

1.1 Blood

Blood is a bodily fluid which performs a number of physiological functions, including the transport of oxygen and nutrients to cells of the body, removal of waste products, and circulation of vital molecules and cells. Furthermore, circulating blood is important for the organism's defense and immune response and plays an essential role in the tissue repair process. Abnormal changes in blood flow are often associated with a broad range of disorders and diseases which include, for instance, hypertension, anemia, atherosclerosis, malaria, and thrombosis. Therefore, understanding of fundamental rheological properties and dynamics of blood cells and blood flow is crucial for many biomedical and bioengineering applications, such as the development of blood substitutes, the design of blood flow assisting devices, and drug delivery. In addition, a detailed understanding of vital blood-related processes in health and disease is likely to result in the development of new effective treatments.

Blood is a suspension of erythrocytes or red blood cells (RBCs), leukocytes or white blood cells (WBCs), thrombocytes or platelets, and various molecules and ions in the blood plasma. RBCs take up about 45% of the total blood volume, WBCs around 0.7%, and the rest corresponds to blood plasma and its substances. One microliter of blood contains about 5×10^6 RBCs, roughly 5000 WBCs, and approximately 2.5×10^5 platelets.

1.2 Blood cells

Figure 1 shows a scanning electron micrograph of blood cells. Human RBCs have a relatively simple structure in comparison to other cells. They have a biconcave shape with an average diameter of approximately $8\,\mu$m and a thickness of about $2\,\mu$m [1]. A RBC membrane consists of a lipid bilayer with an attached cytoskeleton formed by spectrin proteins and linked by short filaments of actin to the bilayer. At the stage of RBC birth, the nucleus and other organelles, which are generally present in eukaryotic cells, are ejected, leaving behind a relatively homogeneous cytosol and no bulk cytoskeleton. RBC cytosol is a hemoglobin-rich solution, which

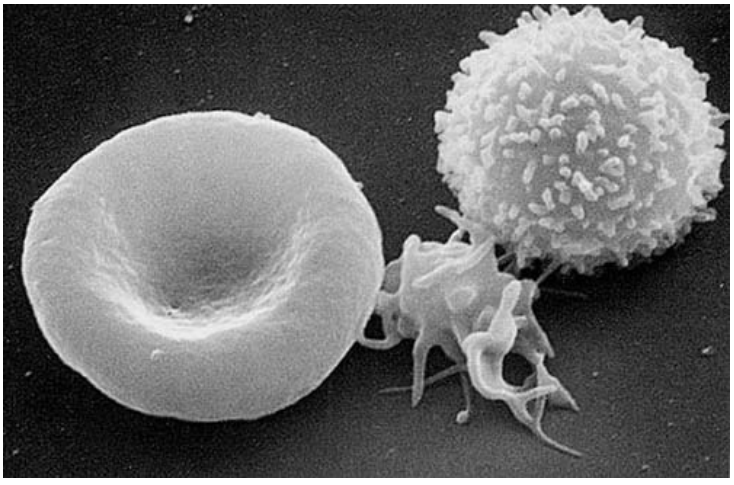

Fig. 1: *A scanning electron micrograph of blood cells. From left to right: a human RBC, activated platelet, and a WBC. Source: The National Cancer Institute at Frederick (NCI-Frederick).*

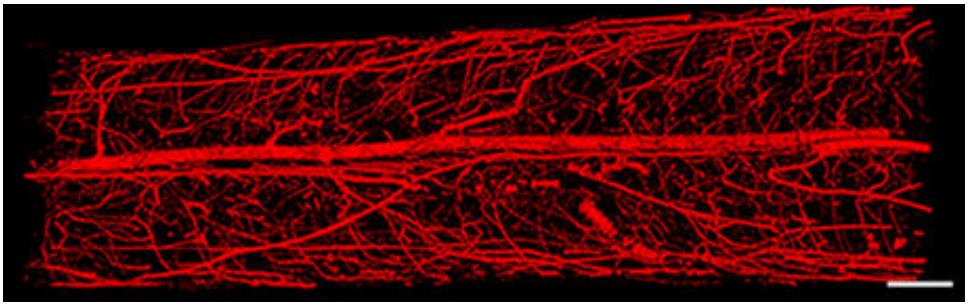

Fig. 2: *3D image of the microvasculature of rat's spinal cord. Reproduced with permission from Ref. [3].*

is able to bind oxygen. Therefore, the main function of RBCs is oxygen delivery to the body tissues. RBCs are very deformable and can pass through capillaries with a diameter several times smaller than the RBC diameter.
WBCs are spherical in shape with a diameter ranging between $7\,\mu$m and $20\,\mu$m, and have one or multiple nuclei. Even though WBCs are stiffer than RBCs, they are able to undergo significant deformation when entering the smallest blood capillaries or transmigrating from blood into the surrounding tissue. WBCs are an important part of the body's immune system. They protect the body against invading bacteria, parasites, and viruses by killing these microorganisms through phagocytic ingestion and other antigen-specific cytotoxic mechanisms. There exist different types of WBCs (e.g., neutrophils, eosinophils, basophils, monocytes, and lymphocytes), each of which is designed for a specific task. WBCs may adhere to the vascular endothelium, which is the first step in their transmigration into the surrounding tissue and a part of the immune response.
Not activated platelets possess a disc-like shape with a diameter ranging between $2\,\mu$m and $4\,\mu$m, and a thickness of about $0.5\,\mu$m [2]. These thin cells have a bulk cytoskeleton, but no nucleus, and play a pivotal role in hemostasis or the blood-clotting process. Upon activation, platelets change their shape by the formation of multiple tethers, as shown in Fig. 1, and become adhesive. The process of adhesion of numerous activated platelets to a blood-vessel injury site results in the formation of a clot (or a plug), which eventually stops bleeding.

1.3 Microcirculation

The microcirculation (or microvascular network) [4, 5] consists of the smallest vessels (i.e., arterioles, capillaries, venules) with diameters up to about $100\,\mu$m. Typically, the microcirculation geometry resembles a tree-like structure (see Fig. 2) formed by microcirculatory vessels, which provide the routes for the circulating blood and enable efficient exchange between blood and the surrounding tissues. Blood flow in microcirculation is extremely complex and diverse with dramatic changes in flow rates and patterns. This complexity is attributed to non-trivial vessel geometries and blood rheological properties [4, 6], which depend on the mechanical properties of blood cells, aggregation interactions, local hematocrit (RBC volume fraction), and flow conditions.
Difficulties with reliable *in vivo* measurements and the complexity of blood flow in microvascular networks in health and disease pose considerable limits on experimental investigations. In contrast, the capabilities of *in silico* modeling to describe the flow behavior of blood in the microcirculation are expanding. Realistic blood flow modeling has a great potential to provide

the necessary theoretical tools to better understand blood flow in normal and diseased microcirculation. Some of these approaches will be discussed further.

1.4 Primary hemostasis

Hemostasis is the process of blood clotting, which is required to stop bleeding at an injury site and initiate wound healing. The start of the hemostatic process is usually referred to as primary hemostasis and corresponds to initial platelet-plug formation at an injury site. Low platelet counts may significantly affect the primary hemostasis, resulting in a substantial increase of bleeding times [7]. Thus, timely and frequent enough platelet adhesion is very important in primary hemostasis. Adhesion of activated platelets is mediated by several receptors at the cell's surface, which can interact with subendothelial components, such as collagen exposed at the damaged vessel wall [8]. Additionally, the adhesion can be supported by other proteins, including the von Willebrand factor (VWF) [7]. The role of VWF in mediating platelet adhesion becomes essential at high shear rates, when platelets are not able to bind to the injury site autonomously.
VWF is a large polymer-like protein made of repeating subunits [9]. It is a shear responsive molecule, because in equilibrium or at low shear rates, VWF remains in a globular configuration due to its internal associations [10], while at high enough shear rates, VWF is able to stretch [11]. In a globular configuration, VWF remains non-adhesive such that its adhesive sites are shielded [12], while in a stretched form, the adhesive sites of VWF get exposed and it can adhere to a damaged endothelium and platelets [10]. After adhering to the damaged endothelium at high shear rates, tethered VWF molecules are able to capture flowing platelets. The VWF-platelet interactions significantly slow down platelets, and facilitate their firm adhesion at the damaged vessel wall. Various VWF dysfunctions can lead to uncontrolled bleeding as in the von Willebrand disease or to spontaneous thrombotic events [13].

2 Methods and models

Modeling blood flow requires the representation of several main components, including fluid flow, blood cells, and suspended molecules (e.g., VWF). Fluid-flow modeling is referred here to a proper representation of the motion of blood plasma and cell's cytosol, resulting in hydrodynamic interactions between suspended cells. Both blood plasma and cell cytosol can be considered to be viscous Newtonian fluids. Fluid flow is modeled by the smoothed dissipative particle dynamics (SDPD) method [14, 15], which is a mesoscopic particle-based simulation approach. Detailed description of the SDPD method can be found in Appendix A.

2.1 Blood cells

RBC membrane is modeled by a set of points $\{\mathbf{x}_i\}$, $i \in 1...N_v$ which are the vertices of a two-dimensional triangulated network on the RBC surface [17, 18], as shown in Fig. 3. The vertices are connected by N_s edges which form N_t triangles. The potential energy of the system is defined as

$$U(\{\mathbf{x}_i\}) = U_s + U_b + U_a + U_v, \tag{1}$$

where U_s is the spring's potential energy to impose membrane shear elasticity, U_b is the bending energy to represent bending rigidity of a membrane, and U_a and U_v stand for the area and

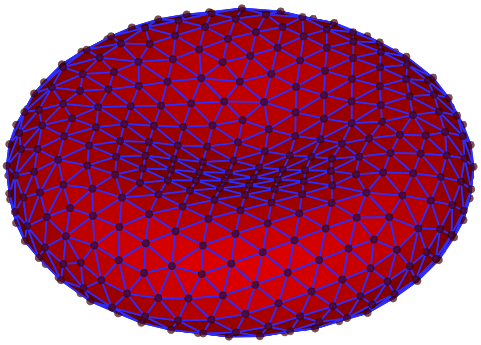

Fig. 3: *Mesoscopic representation of a RBC membrane by a triangular network of bonds. Reproduced with permission from Ref. [16].*

volume conservation constraints, which mimic area-incompressibility of the lipid bilayer and incompressibility of a cytosol, respectively.
The spring's elastic energy mimics the elasticity of the spectrin network, and is given by

$$U_s = \sum_{j \in 1 \ldots N_s} \left[\frac{k_B T l_m (3x_j^2 - 2x_j^3)}{4p(1 - x_j)} + \frac{k_p}{l_j} \right], \tag{2}$$

where l_j is the length of the spring j, l_m is the maximum spring extension, $x_j = l_j / l_m$, p is the persistence length, $k_B T$ is the energy unit, and k_p is the spring constant. The bending energy is defined as

$$U_b = \sum_{j \in 1 \ldots N_s} k_b \left[1 - cos(\theta_j - \theta_0) \right], \tag{3}$$

where k_b is the bending constant, θ_j is the instantaneous angle between two adjacent triangles having the common edge j, and θ_0 is the spontaneous angle.
The area and volume conservation constraints are expressed as

$$\begin{aligned} U_a &= \frac{k_a (A - A_0^{tot})^2}{2A_0^{tot}} + \sum_{j \in 1 \ldots N_t} \frac{k_d (A_j - A_0)^2}{2A_0}, \\ U_v &= \frac{k_v (V - V_0^{tot})^2}{2V_0^{tot}}, \end{aligned} \tag{4}$$

where k_a, k_d and k_v are the global area, local area and volume constraint coefficients, respectively. The terms A and V are the total area and volume of RBC, while A_0^{tot} and V_0^{tot} are the specified total area and volume, respectively. More details on the RBC model can be found in Refs. [18, 19].
Other blood cells, such as WBCs and platelets, can be also represented by the membrane model described above for RBCs [20]. The main differences in comparison to RBCs are the shape and the membrane rigidity, which is normally set to be larger for WBCs and platelets than that for RBCs. More sophisticated models, which explicitly take into account the elasticity of the bulk cytoskeleton, are also available [21].

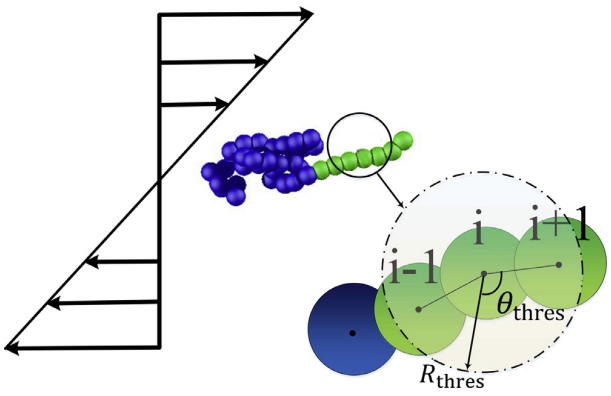

Fig. 4: *Schematic of an attractive polymer with $N = 30$ beads in shear flow. Different bead colors denote non-activated (blue) or activated (green) polymer beads for adhesion. The colors are assigned using the two criteria from Eqs. (7) and (8), which determine a conformation-dependent bead activation for adhesion. Adapted with permission from Ref. [24].*

2.2 von Willebrand factor

VWF is modeled as a shear-activated polymer, which retains its compact shape at low fluid stresses, but is able to stretch at high enough shear rates [11]. The model is based on a bead-spring chain with self-avoiding attractive monomers (see Fig. 4) [22, 23], where beads are connected by springs represented by the finite extensible nonlinear elastic (FENE) potential,

$$U_{\mathrm{FENE}}(r_{ij}) = -\frac{1}{2}k_{\mathrm{s}}l_{\mathrm{max}}^2 \ln\left(1-\left(\frac{r_{ij}}{l_{\mathrm{max}}}\right)^2\right), \tag{5}$$

where k_{s} is the spring stiffness, l_{max} is the maximum spring extension, and r_{ij} is the distance between neighboring beads i and j. Self-avoidance and attractive interactions between beads, which lead to a globular configuration, are modeled by the 12-6 Lennard-Jones (LJ) potential as

$$U_{\mathrm{LJ}}(r_{ij}) = 4\epsilon_{\mathrm{LJ}}\left[\left(\frac{d_{\mathrm{pol}}}{r_{ij}}\right)^{12}-\left(\frac{d_{\mathrm{pol}}}{r_{ij}}\right)^{6}\right], \tag{6}$$

where ϵ_{LJ} is the depth of the potential well, which controls the attraction strength, and d_{pol} is the bead diameter.

In a globular configuration, the polymer remains non-adhesive, while in a stretched state under flow, adhesive interactions with a surface become possible. This activation mechanism is modeled by tracking the degree of local stretching of the polymer in flow [24], as illustrated in Fig. 4. Two geometrical criteria are considered for the bead activation. The first condition corresponds to the angle between two adjacent bonds linking the bead i to its neighboring monomers ($i-1$ and $i+1$), which is directly related to the degree of local stretching of the polymer. Mathematically, it can be expressed as

$$\theta_{i-1,i,i+1} \geq \theta_{\mathrm{thres}} \quad 2 < i < N-1, \tag{7}$$

where θ_{thres} is a threshold angle. Note that this condition is always assumed to be true for the first and the last bead in the polymer. The second criterion monitors the proximity of non-direct neighboring beads within a polymer and is expressed as

$$r_{ij} \geq R_{\mathrm{thres}} \quad j \neq i, i \pm 1, \tag{8}$$

where R_{thres} is a threshold radius. This condition prohibits activation of a polymer bead for adhesion within a globule, even if the condition in Eq. (7) is satisfied. Thus, an inactive bead becomes activated when the two conditions above are satisfied. Similarly, an active bead will be deactivated when one or both criteria are not met.

3 Results

3.1 Fahraeus & Fahraeus-Lindqvist effecs

The basis of our current understanding of microvascular blood flow is mainly formed by two observations, the Fahraeus [25] and the Fahraeus-Lindqvist [26] effects, which have first been found in *in vitro* experiments [25, 26, 27, 28] of blood flow in glass tubes. The Fahraeus effect describes a reduced tube hematocrit in comparison with the discharge hematocrit at the tube exit. Here, the discharge hematocrit is defined as a fraction of RBCs exiting a tube per unit time, while the tube hematocrit corresponds to the volume fraction of RBCs in that tube. The Fahraeus effect arises from the property of RBCs to populate mainly the center of a tube in flow, where they move faster on average than the whole cell suspension (or blood) leading to an increased outflow rate of RBCs measured experimentally. The concentration of RBCs in tube center is a consequence of the migration of RBCs away from vessel walls toward the tube center [29, 30]. This migration is governed by hydrodynamic interactions of RBCs with the walls, which is often referred to as *lift force* in the literature [31, 32]. The Fahraeus effect [25] for single vessels directly implies reduced hematocrit values in microcirculation in comparison with a systemic hematocrit, which has been found experimentally [33, 34]. Following the conservation of blood volume within a closed circulatory system, we can conclude that the hematocrit in microvasculature should be lower than that in large vessels, since RBCs in microcirculation flow faster than the average blood flow.
The second well-known property of flowing blood is the Fahraeus-Lindqvist effect [26], which describes a decrease in the apparent blood viscosity with decreasing tube diameter found in experiments of blood flow in glass tubes [27, 28]. The apparent viscosity is calculated as

$$\eta_{app} = \frac{\pi \Delta p D^4}{128 Q L} = \frac{\Delta p D^2}{32 \bar{v} L}, \tag{9}$$

where D is the tube diameter, Q is the flow rate, and $\Delta p/L$ is the pressure drop in a tube of length L. For higher hematocrits, the apparent viscosity increases, since higher cell crowding leads to a larger flow resistance. For convenience, we define the relative apparent viscosity as

$$\eta_{rel} = \frac{\eta_{app}}{\eta_o}, \tag{10}$$

where η_o is the plasma viscosity. Figure 5 presents simulation results [35] in comparison with the empirical fit to experiments [28] for tube diameters from 10 µm to 40 µm and hematocrit values in the range 0.15 to 0.45. The empirical fit [28] shows that the effective blood viscosity has its minimum in tubes with diameters of about $7 - 8$ µm, while for smaller and larger tube diameters the apparent viscosity is markedly higher. This effect is also directly associated with the property of RBCs to migrate toward the tube center leading to the formation of two phases [29, 30]: a RBC-rich core and a RBC-free layer (RBC-FL) next to the tube walls. The RBC-FL leads to a decrease in the apparent viscosity when its thickness is significant in comparison with the tube diameter, i.e. for not too wide tubes.

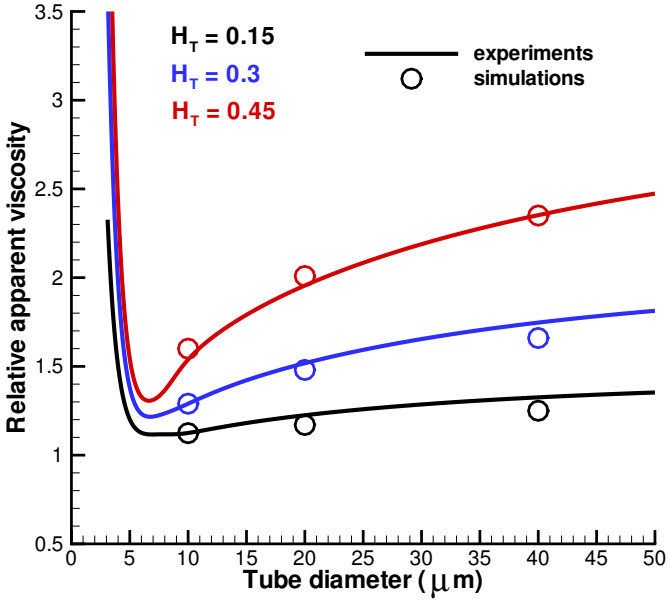

Fig. 5: *Simulated relative apparent viscosity of blood [35] in comparison with experimental data [28] for different hematocrit values and tube diameters. Reproduced with permission from Ref. [16].*

Another effect which may introduce considerable variations of the hematocrit in microcirculation is related to the splitting of RBC volume fraction at bifurcations and branching points [36, 37]. For instance, many side branching vessels may receive only a small fraction of RBCs due to the plasma skimming effect, i.e. such vessels would be fed primarily by blood plasma, since RBCs are located in the center of the feeding vessel. Also, heterogeneous flow rates within the microvasculature result in an elevated hematocrit at daughter vessels with higher flow rates [36, 37]. Thus, the effective discharge hematocrit for a network defined as the flow-weighted mean of the discharge hematocrits in the individual vessels is higher than the simple mean of the individual discharge hematocrits for this vessel network. This property of microcirculatory flow leads to a further reduction of the mean microvascular tube hematocrit and has been referred to as the ”network” Fahraeus effect in the literature [36, 37].

3.2 Margination

Another interesting phenomenon, which takes place in blood flow in the microcirculation is margination of WBCs, platelets, and drug carriers, as illustrated in Fig. 6. Margination is referred to the process of migration of these cells or suspended particles toward vessel walls. In case of WBCs and platelets, the margination process appears to be important for their function, since these cells may need to adhere to vessel walls. Current understanding of the margination process rests on the two mechanisms: (i) particle/cell migration due to hydrodynamic interactions (i.e., lift force) with the walls [31, 32], and (ii) shear-induced diffusion due to collisions/interactions between cells in flow [38, 39, 40]. The former mechanism may lead to the competition between the lift forces on different cells, generally resulting in the effect that more deformable cells (e.g., RBCs) migrate faster away from the wall in comparison to WBCs, for

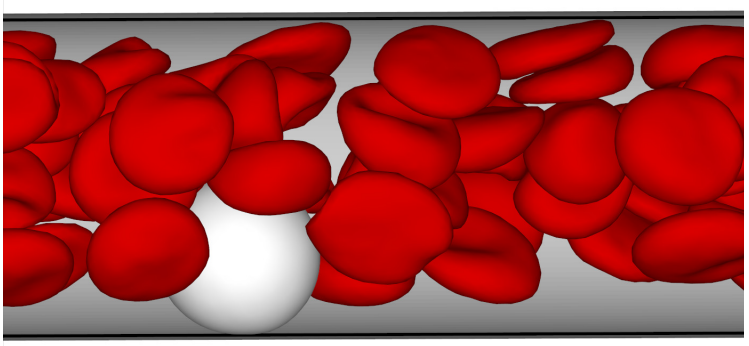

Fig. 6: *A simulation snapshot of RBCs and a marginated WBC at a hematocrit of* 0.3*. The vessel diameter is* 20 *μm and the flow is from the left to the right. Reproduced with permissions from Ref. [20].*

example. The latter mechanism may lead to gradients in the apparent particle/cell diffusivities, which can be interpreted as effective driving forces considering the drift-diffusion formalism [38, 39].
Simulations of WBC margination in blood flow [41, 42, 20] have shown that the most efficient margination of WBCs is achieved at an intermediate range of hematocrits ($H_t = 0.2 - 0.4$) consistent with microcirculatory values [4, 6] and low enough flow rates characteristic for venular blood flow. Margination of platelets has been investigated in a number of numerical studies [43, 38] showing that a certain hematocrit value is required for platelet margination. The margination dynamics of platelets is found to be diffusional [38] in large enough vessels and might be slow in comparison to small vessels such as capillaries. Margination of micro- and nano-particles in blood flow has been also investigated in simulations [44, 45], indicating that microparticles possess much better margination properties in comparison to their nano-scale counterparts.

3.3 VWF adhesion

VWF molecules become adhesive upon stretching [10]. This process is represented by the shear-responsive polymer model described in section 2.2, and activated adhesive beads of the polymer can form bonds with ligands distributed on a wall or platelet surface. The adhesive interactions between two available sites can be formulated as 'chemical' reactions between the unbound and bound states with the rates k_{on} and k_{off} called association and dissociation rates, respectively. The reaction rates determine the frequency of state change, which is modeled by the transition probabilities P_{on} and P_{off} [46] as

$$\frac{\mathrm{d}P_{\text{on}}}{\mathrm{d}t} = -k_{\text{on}} P_{\text{on}}, \text{ if } r \leq r_{\text{cut}}^{\text{on}}, \tag{11}$$

while $P_{\text{on}} = 0$, if $r > r_{\text{cut}}^{\text{on}}$, and

$$\frac{\mathrm{d}P_{\text{off}}}{\mathrm{d}t} = -k_{\text{off}} P_{\text{off}}, \tag{12}$$

where $r_{\text{cut}}^{\text{on}}$ is the cutoff range for bond association. The association rate k_{on} is often assumed to be constant, while k_{off} might be dependent on the force applied to a bond.
It is intuitive that bonds should rupture under strong enough forces and therefore, the slip-bond model assumes that the detachment probability of a bond increases as the applied force on this

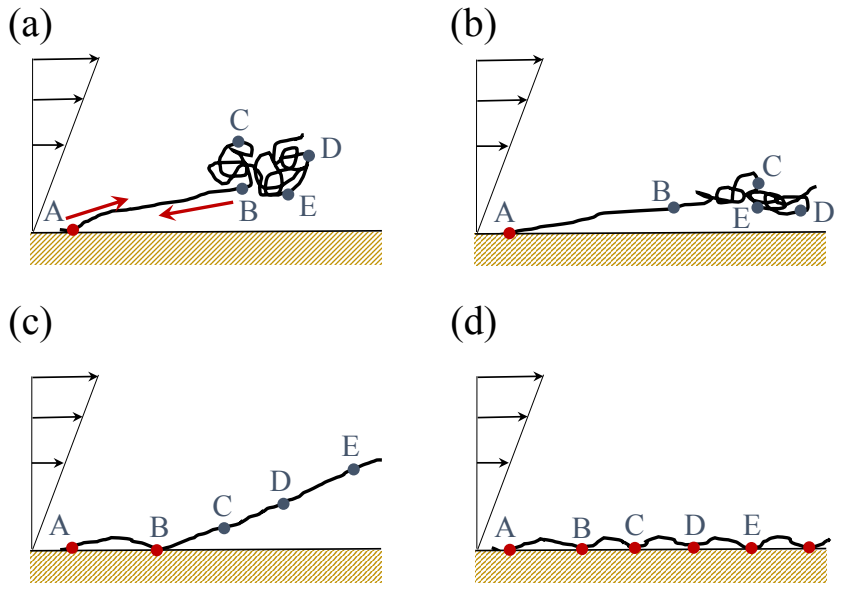

Fig. 7: *Schematic illustration of VWF adhesion to a substrate: (a) formation of initial adhesion to a surface by one of its ends, (b) stretching of an initially tethered VWF, (c) partially adhered chain after stretching, and (d) fully adhered VWF.*

bond is elevated. An alternative characteristic to the detachment probability is the lifetime of a bond, which for a slip bond decreases with increasing applied force. However, the lifetime of certain ligand-receptor interactions may increase as the force is elevated [47, 48] and such bonds are referred to as catch bonds [47]. Clearly, any physical bond will eventually rupture when the applied force becomes large enough. Therefore, the lifetime of an initially catch bond has to start decreasing when a certain value of the applied force is exceeded. As a result, the catch bond behavior should be rather considered as a dual catch-slip behavior. For example, adhesion of VWF to platelet GPIbα receptor exhibits the catch-slip behavior [49, 50].

The stretching of a self-attractive polymer (e.g., VWF) in shear flow starts by pulling a tether from the globule or equivalently one of the polymer ends [23]. Thus, the initial adhesion of VWF is very likely to proceed by binding one of its ends first. Figure 7 illustrates a typical adhesion process of a VWF. At first, one end of a partially stretched polymer adheres to the wall (Fig. 7(a)) and the polymer becomes tethered. Next, the tethered polymer is subjected to significant shear forces exerted by the fluid flow, leading to a further unfolding of the globule (Fig. 7(b)). Note that stretching of an immobilized polymer occurs at much lower shear rates than those required for the stretching of a freely-suspended globule in shear flow [51]. Thus, after initial tethering, unfolding of a globule proceeds rather rapidly (Fig. 7(c)). Following a rapid unfolding of the tethered globule, the VWF exposes new adhesive sites, which can bind to a surface as the shear flow pushes it closer to the wall. Finally, the VWF chain fully adheres (Fig. 7(d)).

It is important to emphasize that the formation of an initial adhesion (Fig. 7(a)) plays a deciding role for the overall adhesion to a surface. Clearly, this initial interaction has to be strong enough, and the formed bonds need to possess a long enough lifetime in order to sustain large forces exerted by the fluid flow and to allow enough time for polymer stretching and further adhesion to occur. Therefore, this process has to be facilitated by a relatively fast association rate and need to involve preferentially a catch-like bond behavior. In fact, recent simulations [52] suggest

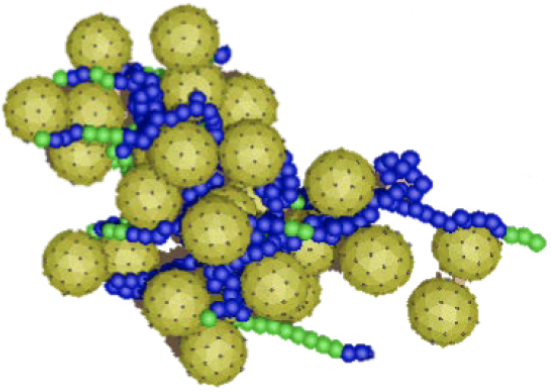

Fig. 8: *An aggregate formed by spherical particles (mimicking platelets) and VWF chains. Such aggregates form at high enough shear rates and are reversible when the flow is stopped.*

that the adhesion of VWF to a surface at high shear rates is controlled by long-lived (catch-like) bonds. Similarly, adsorption of homopolymeric globules to a surface has been found to be enhanced at high shear rates by catch-bond interactions [53].
A very interesting behavior of VWF is the dissociation of VWF-platelet aggregates, which form at high shear rates, but disaggregate when the flow is stopped [49, 54]. Thus, adhesion of VWF is reversible under flow cessation. An adhered polymer with catch-slip surface interactions remains stable in shear flow unless the shear stresses become very large or equivalently when formed bonds stretch significantly such that they reach their slip part, where the lifetime strongly drops. At an intermediate shear stress, most of the bonds actually have very long lifetime due to the catch part of bond interactions. When the shear stress is removed by stopping the flow, the adhesive bonds return to their nearly unstressed state, and their lifetime significantly drops because of their catch-bond characteristic. Hence, the polymer starts losing its bonds to the substrate and forms a globule, mainly due to its internal attractive interactions. Eventually, the globule completely dissociates from the surface, since all polymer beads become inactive.

3.4 VWF-platelet aggregates

Similarly to the VWF adhesion at a wall, VWF chains bind to flowing platelets, resulting in the formation of VWF-platelet aggregates, as illustrated in Fig. 8. Aggregate formation is supported by the rotational motion in shear flow, which facilitates the wrapping of stretched and adhesive VWFs around platelets. Here, also high enough stresses are required for the activation of VWF. Furthermore, these aggregates are reversible and they dissociate when the flow strength is reduced or the flow is stopped. The reversibility of aggregates is directly associated with the reversible adhesion of VWF discussed in section 3.3.

3.5 Blood flow in microcirculation

Blood-flow modeling on the level of single cells in large microvascular networks still remains very limited. In order to overcome these problems, current models of blood flow in microcirculation [55, 56] implement a network approach of a coupled system of Poiseuille-flow equations in individual segments of the microvasculature. Thus, following the Poiseuille law the conduc-

tance G of each segment can be described similar to Eq. (9) as

$$G = \frac{Q}{\Delta p} = \frac{\pi D^4}{128 \eta L}, \tag{13}$$

where η is the fluid's dynamic viscosity. In a network, mass conservation (the sum of inflows must be equal to the sum of outflows) is employed to obtain the equations

$$\sum_{i,j=1}^{N} Q_{ij} = \sum_{i,j=1}^{N} G_{ij}(p_i - p_j) = 0, \tag{14}$$

where p_i is the pressure at different segment nodes (e.g., bifurcations, vessel junctions), Q_{ij} is the flow rate at a segment (i, j), and G_{ij} is its hydraulic conductance. Such a system of equations also requires consistent boundary conditions at all inflows and outflows of the selected network.

The hydraulic conductance G_{ij} is defined through the parameters D_{ij}, L_{ij}, and η_{ij}, where the diameters and lengths of segments simply come from a geometrical structure of the network of interest. As a first approximation, a constant viscosity in all segments could be assumed; however, in practice, this assumption is far from realistic due to significant hematocrit heterogeneities within a vessel network. Therefore, a better assumption is to make η_{ij} hematocrit dependent with the values following the empirical fits to available experimental data [28]. The appearance of hematocrit as a new variable in this system of equations implies that we have to determine physical separation of blood cells at branching points or equivalently to define bifurcation laws. Currently, the state of the art for the bifurcation laws is based on a phenomenological model, which is an average fit to available experimental data [6].

4 Conclusions

Theoretical models of blood flow in microvasculature are very powerful tools, because they are able to represent blood flow in a large network of vessels and capture various microcirculatory processes. However, these models depend entirely on the input assumptions which include blood-viscosity dependence, bifurcation laws, margination effects, 'non-hydrodynamic' processes (e.g., the adhesion of WBCs, platelets, and VWF), etc. This input should ideally come from experimental measurements to make the blood-flow simulations realistic. Even though some experimental data about the mean blood-flow characteristics are readily available, a systematic and detailed description of blood flow properties in microvasculature requires new experimental measurements in real and/or artificial microvascular networks, which can provide the basis for model validation. Furthermore, the combination of a detailed model on the level of single cells and a simplified model capable of capturing blood flow in a large microvascular network appears to be very promising. The integration of these different approaches may make it possible to build advanced blood-flow models capable of describing realistically the flow in microcirculation.

Appendices

A Smoothed dissipative particle dynamics

The original smoothed dissipative particle dynamics (SDPD) method [14] is derived through a Lagrangian discretization of the Navier-Stokes (NS) equations similar to the smoothed particle hydrodynamics method [57], while thermal fluctuations in SDPD are introduced similarly to the dissipative particle dynamics method [58, 59]. Each SDPD particle represents a small volume of fluid, instead of individual atoms or molecules, and corresponds to a thermodynamically consistent and well-defined physical volume [60]. The original SDPD method [14] does not conserve angular momentum, which might be crucial for some problems. A more general version of the SDPD method with angular momentum conservation [15] has been proposed recently, where every particle possesses a spin variable $\boldsymbol{\omega}$ and a moment of inertia I in addition to its mass m, coordinate $\mathbf{r}$, and linear velocity $\mathbf{v}$. The new SDPD method [15] is obtained by a Lagrangian discretization of the continuity equation and the NS equation with spin [61].
Particle interactions in the SDPD method with angular momentum conservation [15] are represented by three deterministic forces (conservative (C), translational dissipative (D), and rotational dissipative (R)) and a random force ($\sim$) given by

$$\begin{aligned}
\mathbf{F}^C_{ij} &= \left(\frac{p_i}{\rho_i^2} + \frac{p_j}{\rho_j^2}\right) F_{ij}\mathbf{r}_{ij},\\
\mathbf{F}^D_{ij} &= -\gamma_{ij}\left(\mathbf{v}_{ij} + \mathbf{n}_{ij}(\mathbf{n}_{ij}\cdot\mathbf{v}_{ij})\right),\\
\mathbf{F}^R_{ij} &= -\gamma_{ij}\frac{\mathbf{r}_{ij}}{2}\times(\boldsymbol{\omega}_i + \boldsymbol{\omega}_j),\\
\tilde{\mathbf{F}}_{ij} &= \sigma_{ij}\left(d\overline{\boldsymbol{\mathcal{W}}}^S_{ij} + \frac{1}{3}tr[d\boldsymbol{\mathcal{W}}_{ij}]\mathbb{1}\right)\cdot\frac{\mathbf{n}_{ij}}{\delta t},
\end{aligned} \tag{15}$$

where p is the particle pressure, which follows a selected equation of state, ρ is the particle density obtained as $\rho_i = \sum_{j=1}^{N} m_j W_{ij}$ for particle i with $W_{ij} = W(\mathbf{r}_{ij}) = W(\mathbf{r}_i - \mathbf{r}_j, h)$ being an interpolation kernel, h the smoothing radius, and $\nabla_i W_{ij} = -\mathbf{r}_{ij}F_{ij}$. Furthermore, $\mathbf{n}_{ij} = \mathbf{r}_{ij}/|\mathbf{r}_{ij}|$, $\gamma_{ij} = 20\eta F_{ij}/(7\rho_i\rho_j)$ is the dissipative coefficient, $\sigma_{ij} = 2\sqrt{\gamma_{ij}k_BT}$ is the random coefficient with T being the temperature and k_B the Boltzmann constant. $\boldsymbol{\mathcal{W}}_{ij}$ is a matrix of independent Wiener increments, $tr[d\boldsymbol{\mathcal{W}}_{ij}]$ is its trace, $d\overline{\boldsymbol{\mathcal{W}}}^S_{ij}$ is the traceless symmetric part, $\mathbb{1}$ is the unity matrix, and δt is the integration time step.
The forces in Eq. (15) lead to torques $\mathbf{L}_{ij}$ acting on a particle i from surrounding particles j given by $\mathbf{L}_{ij} = \frac{1}{2}\mathbf{r}_{ij}\times\mathbf{F}_{ij}$. The equation of motion for a particle i is described by the Newton's second law as

$$\dot{\mathbf{r}}_i = \mathbf{v}_i, \qquad \dot{\mathbf{v}}_i = \sum_j \frac{1}{m_j}\mathbf{F}_{ij}, \qquad \dot{\boldsymbol{\omega}}_i = \sum_j \frac{1}{I_j}\mathbf{L}_{ij}. \tag{16}$$

Time evolution of particle positions, translational and angular velocities is integrated using the velocity-Verlet algorithm [62].

References

[1] Y. C. Fung, *Biomechanics: Mechanical properties of living tissues* (Springer-Verlag, New York, 1993), 2nd ed.
[2] G. Pocock, C. D. Richards, and D. A. Richards, *Human physiology* (Oxford University Press, 2006).
[3] Y. Cao, T. Wu, Z. Yuan, D. Li, S. Ni, J. Hu, and H. Lu, Sci. Rep. **5**, 12643 (2015).
[4] A. S. Popel and P. C. Johnson, Annu. Rev. Fluid Mech. **37**, 43 (2005).
[5] T. W. Secomb and A. R. Pries, J. Physiol. **589**, 1047 (2011).
[6] A. R. Pries, T. W. Secomb, and P. Gaehtgens, Cardiovasc. Res. **32**, 654 (1996).
[7] A. J. Reininger, Haemophilia **14**, 11 (2008).
[8] B. P. Nuyttens, T. Thijs, H. Deckmyn, and K. Broos, Thromb. Res. **127**, S26 (2011).
[9] W. E. Fowler, L. J. Fretto, K. K. Hamilton, H. P. Erickson, and P. A. McKee, J. Clin. Invest. **76**, 1491 (1985).
[10] T. A. Springer, Blood **124**, 1412 (2014).
[11] S. W. Schneider, S. Nuschele, A. Wixforth, C. Gorzelanny, A. Alexander-Katz, R. R. Netz, and M. F. Schneider, Proc. Natl. Acad. Sci. USA **104**, 7899 (2007).
[12] H. Ulrichts, M. Udvardy, P. J. Lenting, I. Pareyn, N. Vandeputte, K. Vanhoorelbeke, and H. Deckmyn, J. Biol. Chem. **281**, 4699 (2006).
[13] R. Schneppenheim, U. Budde, F. Oyen, D. Angerhaus, V. Aumann, E. Drewke, W. Hassenpflug, J. Häberle, K. Kentouche, E. Kohne, K. Kurnik, D. Mueller-Wiefel, *et al.*, Blood **101**, 1845 (2003).
[14] P. Español and M. Revenga, Phys. Rev. E **67**, 026705 (2003).
[15] K. Müller, D. A. Fedosov, and G. Gompper, J. Comp. Phys. **281**, 301 (2015).
[16] D. A. Fedosov, H. Noguchi, and G. Gompper, Biomech. Model. Mechanobiol. **13**, 239 (2014).
[17] H. Noguchi and G. Gompper, Proc. Natl. Acad. Sci. USA **102**, 14159 (2005).
[18] D. A. Fedosov, B. Caswell, and G. E. Karniadakis, Biophys. J. **98**, 2215 (2010).
[19] D. A. Fedosov, B. Caswell, and G. E. Karniadakis, Comput. Meth. Appl. Mech. Eng. **199**, 1937 (2010).
[20] D. A. Fedosov and G. Gompper, Soft Matter **10**, 2961 (2014).
[21] M. L. Rodriguez, P. J. McGarry, and N. J. Sniadecki, Appl. Mech. Rev. **65**, 060801 (2013).
[22] A. Alexander-Katz, M. F. Schneider, S. W. Schneider, A. Wixforth, and R. R. Netz, Phys. Rev. Lett. **97**, 138101 (2006).
[23] A. Alexander-Katz and R. R. Netz, Macromolecules **41**, 3363 (2008).
[24] B. Huisman, M. Hoore, G. Gompper, and D. A. Fedosov, Med. Eng. Phys. **48**, 14 (2017).
[25] R. Fåhraeus, Physiol. Rev. **9**, 241 (1929).
[26] R. Fåhraeus and T. Lindqvist, Am. J. Phys. **96**, 562 (1931).
[27] W. Reinke, P. Gaehtgens, and P. C. Johnson, Am. J. Physiol. **253**, H540 (1987).
[28] A. R. Pries, D. Neuhaus, and P. Gaehtgens, Am. J. Physiol. **263**, H1770 (1992).
[29] H. L. Goldsmith, G. R. Cokelet, and P. Gaehtgens, Am. J. Physiol. **257**, H1005 (1989).
[30] G. R. Cokelet and H. L. Goldsmith, Circ. Res. **68**, 1 (1991).
[31] I. Cantat and C. Misbah, Phys. Rev. Lett. **83**, 880 (1999).
[32] M. Abkarian, C. Lartigue, and A. Viallat, Phys. Rev. Lett. **88**, 068103 (2002).
[33] B. Klitzman and B. R. Duling, Am. J. Physiol. **237**, H481 (1979).
[34] G. W. Schmid-Schönbein, R. Skalak, S. Usami, and S. Chien, Microvasc. Res. **19**, 18 (1980).

[35] D. A. Fedosov, B. Caswell, A. S. Popel, and G. E. Karniadakis, Microcirculation **17**, 615 (2010).
[36] A. R. Pries, K. Ley, and P. Gaehtgens, Am. J. Physiol. **251**, H1324 (1986).
[37] A. R. Pries, K. Ley, M. Claassen, and P. Gaehtgens, Microvasc. Res. **38**, 81 (1989).
[38] H. Zhao, E. S. G. Shaqfeh, and V. Narsimhan, Phys. Fluids **24**, 011902 (2012).
[39] A. Kumar, R. G. Henriquez-Rivera, and M. D. Graham, J. Fluid Mech. **738**, 423 (2014).
[40] K. Vahidkhah, S. L. Diamond, and P. Bagchi, Biophys. J. **106**, 2529 (2014).
[41] J. B. Freund, Phys. Fluids **19**, 023301 (2007).
[42] D. A. Fedosov, J. Fornleitner, and G. Gompper, Phys. Rev. Lett. **108**, 028104 (2012).
[43] L. Crowl and A. L. Fogelson, J. Fluid Mech. **676**, 348 (2011).
[44] K. Müller, D. A. Fedosov, and G. Gompper, Sci. Rep. **4**, 4871 (2014).
[45] S. Fitzgibbon, A. P. Spann, Q. M. Qi, and E. S. G. Shaqfeh, Biophys. J. **108**, 2601 (2015).
[46] G. I. Bell, Science **200**, 618 (1978).
[47] M. Dembo, D. C. Torney, K. Saxman, and D. Hammer, Proc. R. Soc. Lond. B **234**, 55 (1988).
[48] F. Kong, A. J. García, A. P. Mould, M. J. Humphries, and C. Zhu, J. Cell. Biol. **185**, 1275 (2009).
[49] T. A. Doggett, G. Girdhar, A. Lawshé, D. W. Schmidtke, I. J. Laurenzi, S. L. Diamond, and T. G. Diacovo, Biophys. J. **83**, 194 (2002).
[50] J. Kim, C.-Z. Zhang, X. Zhang, and T. A. Springer, Nature **466**, 992 (2010).
[51] C. E. Sing and A. Alexander-Katz, Macromolecules **44**, 9020 (2011).
[52] C. E. Sing, J. G. Selvidge, and A. Alexander-Katz, Biophys. J. **105**, 1475 (2013).
[53] M. Radtke and R. R. Netz, Eur. Phys. J. E **38**, 69 (2015).
[54] H. Chen, M. A. Fallah, V. Huck, J. I. Angerer, A. J. Reininger, S. W. Schneider, M. F. Schneider, and A. Alexander-Katz, Nat. Commun. **4**, 1333 (2013).
[55] A. R. Pries, T. W. Secomb, T. Gessner, M. B. Sperandio, J. F. Gross, and P. Gaehtgens, Circ. Res. **75**, 904 (1994).
[56] A. R. Pries, T. W. Secomb, P. Gaehtgens, and J. F. Gross, Circ. Res. **67**, 826 (1990).
[57] J. J. Monaghan, Rep. Prog. Phys. **68**, 1703 (2005).
[58] P. J. Hoogerbrugge and J. M. V. A. Koelman, Europhys. Lett. **19**, 155 (1992).
[59] P. Español and P. Warren, Europhys. Lett. **30**, 191 (1995).
[60] A. Vázquez-Quesada, M. Ellero, and P. Español, J. Chem. Phys. **130**, 034901 (2009).
[61] D. W. Condiff and J. S. Dahler, Phys. Fluids **7**, 842 (1964).
[62] M. P. Allen and D. J. Tildesley, *Computer simulation of liquids* (Clarendon Press, New York, 1991).